Domains of electrically induced valley polarization in two-dimensional Dirac semiconductors

V. A. Kochelap,[1] V. N. Sokolov,[1,*] and K. W. Kim[2,3]

[1]*Department of Theoretical Physics, Institute of Semiconductor Physics, NASU, Pr. Nauki 41, Kiev 03028, Ukraine*

[2]*Department of Electrical and Computer Engineering, North Carolina State University, Raleigh, North Carolina 27695, USA*

[3]*Department of Physics, North Carolina State University, Raleigh, North Carolina 27695, USA*

(Received 26 March 2021; revised 15 July 2021; accepted 15 July 2021; published 3 August 2021)

Electrically induced formation of valley-polarized free-carrier domains is theoretically investigated in two-dimensional (2D) honeycomb lattice systems exhibiting topological valley transport and the valley Hall effect. The results show that under a strong electric field E applied along a nanostrip, the domains can be formed across the strip when this transverse dimension is comparable to the intervalley diffusion length L_{iv}. Further, these domains are found to be characterized by two distinct length scales dependent on E and L_{iv}, i.e., the *extended* diffusion length $L_{\rm ext}$ ($\propto L_{iv}E$) and the *compressed* diffusion length $L_{\rm com}$ ($\propto L_{iv}/E$). The former determines the extension of the domain plateaus, whereas the latter specifies the width of the domain wall. Within each of the domains (excluding a narrow region of the domain wall; $L_{\rm ext} \gg L_{\rm com}$), the charge carriers are fully polarized belonging to only one of the valleys, providing a pure bulk valley current inside the considered domain region. The domain properties including the polarization amplitude and domain wall position are analyzed as a function of the applied electric field and intervalley scattering rates at the edges. The position of the domain wall, which determines the relative extension of the plateaus, can be controlled by a transverse current flowing between the Hall-type contacts. The current-voltage characteristic demonstrates a superlinear behavior in the range of electric fields corresponding to the valley-polarization domain formation. This feature is a distinctive signature of the anomalous transport arising from Bloch-band Berry curvature, which enhances the longitudinal conductance and diminishes the channel resistance. By reversing the applied electric field, the valley polarization and localization of the valley-polarized currents can be abruptly switchable. We suggest that the studied scheme of electrically induced domains of valley polarization in the 2D honeycomb lattice systems can be used in novel applications with all-electrical control and manipulation of the valley degree of freedom.

DOI: 10.1103/PhysRevB.104.075403

I. INTRODUCTION

During the last decade, there have been growing interests in the field of valleytronics (i.e., valley-dependent electronics and optoelectronics [1–3]) motivated by exploiting the valley degree of freedom of the charge carriers [4] in the multivalley semiconductor systems for information processing and storage similar to the spin counterpart in spintronics [5]. Evidently, a key aspect of this field is the ability to selectively generate, manipulate, and detect valley-polarized charge carriers and electrical currents. Such an ability for valley polarization has already been reported in the experiments with traditional multivalley three-dimensional (3D) semiconductors (e.g., Ge [6], diamond [7], and Bi [8]) as well as with the quasi-two-dimensional (quasi-2D) structures [e.g., AlAs quantum wells (QWs) [9] and ultrahigh mobility Si (111) heterostructures [10,11]]. By contrast the recent focus, driven by the emergence of graphene, has been on 2D honeycomb lattice systems with broken inversion symmetry [12–19]. This has led to the extension not only of relevant 2D material systems [20–24], but also of valley physics related to the Berry phase [25–27]. The feasibility of valley-based quantum computing has also been explored for donor states in Si [28,29] and graphene quantum dots [30]. It should be noted that among different ways of creating valley polarization (for instance, an external force by an electrical [6,7] or magnetic field [8], circularly polarized light [15], effective fields via the proximity interaction [31], and various types of strain [32–35]), the pure electrical methods are the most preferable for potential applications [1]. Recently, an electrical method has been explored to induce and control the valley magnetic domains in a uniaxially strained and biased electron-doped monolayer MoS_2 and bilayer MoS_2 under a vertical electric field in a ribbon geometry [35,36].

One possible way for electrical generation and control of valley polarization is to use the inherent band-structure anisotropy of various valleys, wherein the valley current flows at an angle to the applied electric field. In a nanostrip geometry with a finite width, an in-plane electric field applied along the strip causes the carriers of different valleys to flow toward the opposite edges where they accumulate and thereby create well-resolved spatial regions (domains) of strong valley polarization. Here, a distinction needs to be made between the two physical mechanisms leading to valley polarization. More specifically, the electrical valley anisotropy can be caused by (i) valley-dependent anisotropic effective-mass energy spectra (as in n-Ge and n-Si [37]); and

*sokolov@isp.kiev.ua

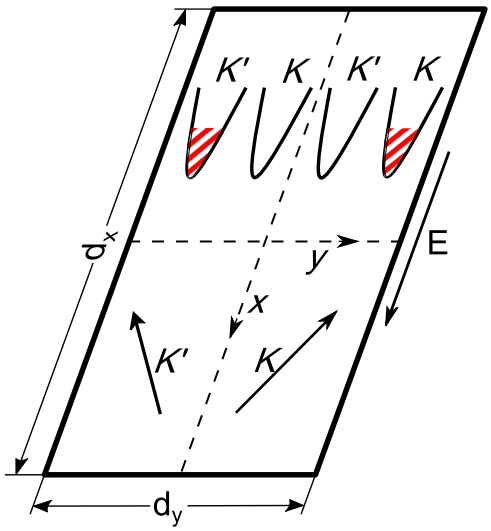

FIG. 1. Schematic illustration of the sample geometry for the electrically induced valley-polarization domains. When the external electric field E increases, the valleys K and K' are asymmetrically occupied due to the size effect on the intervalley diffusion length ($d_y \sim L_{iv}$). The skewed arrows K and K' depict the electron flows to the sample edges under the valley Hall effect.

(ii) topological Berry-phase effects in the crystals of normally isotropic valleys but with no inversion symmetry. Examples of the latter include gapped graphene and group-VI semiconducting transition-metal dichalcogenides (TMDs) [38]. As indicated above, we focus on the 2D Dirac semiconductors with broken inversion symmetry. Accordingly, the aforementioned electrical anisotropy schematically illustrated in Fig. 1 is a consequence of the Berry-phase supported topological transport giving rise to the valley Hall effect [15,38–41].

The rest of this paper is organized as follows. In Sec. II, our theoretical model and basic equations are introduced for drift-diffusion transport of the carriers, which include both normal (diagonal) and anomalous (off-diagonal) topological contributions to the kinetic coefficients. It is shown that the obtained system of nonlinear equations, which describes the valley polarization in 2D samples with restricted transverse dimensions, can be transformed into a universal form without parameters; its solutions, taking into account the boundary conditions at the sample edges, are classified generally by the phase-plane analysis. In Sec. III, it is demonstrated by numerical calculations and analytical results that the increasing strength of the applied electric field leads to the formation of well-resolved spatial domains of valley polarization. The position of the domain wall is examined in terms of the boundary conditions imposed at the edges. The results clearly reveal a superlinear current-voltage characteristic in the field range where the domains are formed. An attempt is also made in Sec. IV to go beyond the treatment based on the quasineutrality condition. Specifically, the Poisson equation is solved here to evaluate the correction to the valley polarization due to the excess charges. The discussions on the obtained results are provided in Sec. V, which is followed by a brief summary at the end.

II. THEORETICAL MODEL

To analyze the behavior of nonequilibrium free carriers (electrons or holes) under the valley Hall effect (VHE), we use a drift-diffusion model for carrier transport in a semiconductor 2D strip, with in-plane dimensions $d_x \gg d_y = 2d$, in an external electric field $E_x = E > 0$ applied in the x direction (Fig. 1). Due to the particular sample geometry, all physical quantities analyzed below can be considered to be homogeneous along the channel length, independent of the x coordinate. In a steady state, the continuity equations can be used to express the transverse distributions of the carrier densities $n_K(y)$ and $n_{K'}(y)$ in the K and K' valleys induced by the electric current flowing in the x direction, i.e.,

$$0 = -\frac{n_K - n_{K'}}{\tau_{KK'}} - \frac{di_y^K}{dy},$$
$$0 = -\frac{n_{K'} - n_K}{\tau_{K'K}} - \frac{di_y^{K'}}{dy}. \tag{1}$$

Here, $\tau_{KK'} = \tau_{K'K} = \tau$ is the intervalley scattering time and the carrier flux densities $i_y^{K(K')}(y)$ can be written as

$$i_y^\alpha = -\mu_{yx}^\alpha n_\alpha E_x - \mu_{yy}^\alpha n_\alpha E_y - D_{yy}^\alpha \frac{dn_\alpha}{dy} \tag{2}$$

with the valley index $\alpha = (K, K')$, the tensor mobility μ_{ij}^α, and the diffusivity D_{ij}^α. The two tensors are related through the Einstein relationship [42], and possess the following symmetry properties: $\mu_{xx}^\alpha = \mu_{yy}^\alpha = \mu$, $D_{xx}^\alpha = D_{yy}^\alpha = D$ for the diagonal components, and $\mu_{yx}^{K'} = -\mu_{yx}^K$, $\mu_{yx}^\alpha = -\mu_{xy}^\alpha$ and $D_{yx}^{K'} = -D_{yx}^K$, $D_{yx}^\alpha = -D_{xy}^\alpha$ for the off-diagonal components [43]. The latter are the consequence of the Berry-phase effects, the anomalous velocity of carriers resulting from the presence of Berry curvature.

In the analysis, it is convenient to exploit the fact that the splitting between the K and K' valleys does not affect the total charge carrier density N. Assuming that N is nearly uniform across the nanostrip width (i.e., the quasineutrality condition with no or little net charge fluctuation), we can obtain

$$n_K(y) + n_{K'}(y) = N. \tag{3}$$

Further, an additional condition $i_y(y = \pm d) = 0$ can be imposed since no carrier current $i_y = i_y^K + i_y^{K'}$ flows across the edges at $y = \pm d$; this leads to $i_y(y) = 0$ when accounting for $\nabla \cdot \mathbf{i} = 0$ ($\mathbf{i} = i_x\hat{\mathbf{x}} + i_y\hat{\mathbf{y}}$). Then, the induced transverse electric field can be determined from Eqs. (2) and (3) as

$$E_y = \frac{\mu_{xy}^K}{\mu_{yy}^K} \frac{n_K - n_{K'}}{n_K + n_{K'}} E_x. \tag{4}$$

Subsequent substitution of i_y^α into Eq. (1) yields

$$\mu_{yy}^K \frac{d}{dy}[(n_K - n_{K'})E_y] + D_{yy}^K \frac{d^2}{dy^2}(n_K - n_{K'}) = \frac{n_K - n_{K'}}{\tau/2}. \tag{5}$$

Thus, a closed system of expressions [Eqs. (3)–(5)] are obtained for the electron densities n_K, $n_{K'}$ in different valleys and the induced electric field E_y. These equations must be supplemented with the boundary conditions (BCs) at the edges. The

suitable BCs can be chosen in the form

$$i_y^K(y=\pm d) = \pm s_{KK'}^{\pm}(n_K^{\pm} - n_{K'}^{\pm}),$$
$$i_y^{K'}(y=\pm d) = \pm s_{K'K}^{\pm}(n_{K'}^{\pm} - n_K^{\pm}), \tag{6}$$

where $s_{KK'}^{\pm} = s_{K'K}^{\pm} = s^{\pm}$ and $n_{K,K'}^{\pm}$ are the intervalley scattering rates and the valley carrier densities at the edges $y = \pm d$, respectively. Note that there are two key figures of merit arising as a consequence of the Berry-phase effects; i.e., the carrier transport anisotropy $a = \mu_{xy}^K/\mu_{yy}^K = D_{xy}^K/D_{yy}^K$ and the induced valley polarization $P = (n_K - n_{K'})/N$. From Eq. (3), it follows that $n_K = N(1+P)/2$ and $n_{K'} = N(1-P)/2$.

Further, it is convenient to use dimensionless variables $\zeta = y/L_{iv}$, $P = P(\zeta)$ and parameters $\mathcal{E}_{x,y} = E_{x,y}/E_c$, $S^{\pm} = 2s^{\pm}L_{iv}/D$, where $L_{iv} = (D\tau/2)^{1/2}$ is the intervalley diffusion length and $E_c = k_BT/ae_0L_{iv}$ is the characteristic critical electric field (k_B is the Boltzmann constant, T is the temperature, and e_0 is unit charge which is taken to be positive). In addition, the dimensionless width of the conducting channel can be defined as $2\delta = d_y/L_{iv}$ ($-\delta \leqslant \zeta \leqslant \delta$). Then, the transverse electric field [Eq. (4)] is expressed as

$$\mathcal{E}_y(\zeta) = aP(\zeta)\mathcal{E}_x. \tag{7}$$

The system of Eqs. (3)–(6) is reduced to one nonlinear differential equation of the second order governing the valley polarization

$$\frac{d^2P}{d\zeta^2} + \mathcal{E}_x\frac{dP^2}{d\zeta} - P = 0, \tag{8a}$$

$$\left[\frac{dP}{d\zeta} - (1-P^2)\mathcal{E}_x \pm S^{\pm}P\right]_{\zeta=\pm\delta} = 0. \tag{8b}$$

The explicit dependencies of $P(\zeta)$, $\mathcal{E}_y(\zeta)$, and $n_{K,K'}(\zeta)$ can be calculated for given values of $\mathcal{E}_x$ and $S^{\pm}$ by numerical solution of Eqs. (8a) and (8b). To this end, Eq. (8a) is transformed, by using the substitution $\bar{P} = P\mathcal{E}_x$, to a universal form (with no parameters)

$$\frac{d^2\bar{P}}{d\zeta^2} + \frac{d\bar{P}^2}{d\zeta} - \bar{P} = 0, \tag{9a}$$

with the BCs

$$\left[\frac{d\bar{P}}{d\zeta} - (\mathcal{E}_x^2 - \bar{P}^2) \pm S^{\pm}\bar{P}\right]_{\zeta=\pm\delta} = 0. \tag{9b}$$

In addition, $\mathcal{E}_y(\zeta) = a\bar{P}(\zeta)$.

Noting that Eq. (9a) does not contain independent variable ζ explicitly, it is clear that its solutions can be fully classified by an analytical phase-plane examination [44]. The phase-plane $(\bar{p}, \bar{P})$ behavior is determined by the equation

$$\frac{d\bar{p}}{d\bar{P}} = \bar{P}\frac{1-2\bar{p}}{\bar{p}}, \tag{10a}$$

where $\bar{p} = d\bar{P}/d\zeta$. In the linear approximation, it gives the eigenvalues $\lambda_{1,2} = \pm 1$, which correspond to one singular (a *saddle*) point ($\bar{p} = 0, \bar{P} = 0$). In addition, also seen is a singular solution $\bar{p} = \frac{1}{2}$. The phase trajectories $\bar{p} = \bar{p}(\bar{P})$ are found immediately in an implicit form as

$$\bar{P}^2 + \frac{d\bar{P}}{d\zeta} + \frac{1}{2}\ln\left|2\frac{d\bar{P}}{d\zeta} - 1\right| = \bar{C}. \tag{10b}$$

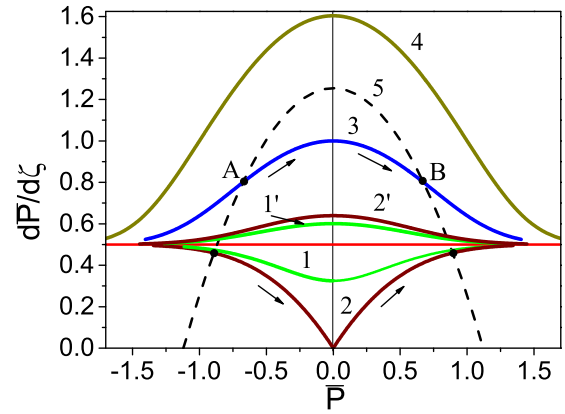

FIG. 2. Phase portrait of Eq. (9a). Integral curves are shown for different values of integration constant $\bar{C}$: curves 1, 1′, $\bar{C} = -0.2$; 2, 2′, $\bar{C} = 0$; 3, $\bar{C} = 1$; 4, $\bar{C} = 2$. Dashed line 5 is for the BCs with $S^{\pm} = 0$ ($\mathcal{E}_x^2 = 1.25$). Arrows indicate the direction of motion along the integral curves with increasing ζ. Two portions of curve 2 ($\bar{P} \gtrless 0$) correspond to wide (semi-infinite) samples.

Figure 2 illustrates $(\frac{d\bar{P}}{d\zeta}, \bar{P})$-phase portrait of the solutions to Eq. (9a). Despite the simplicity of Eq. (9a), the phase portrait is characterized by a few remarkable features. Indeed, for the same integration constant $\bar{C}$, there exist two corresponding integral curves (phase trajectories). Examples are curves 1, 1′ for $\bar{C} = -0.2$ and 2, 2′ for $\bar{C} = 0$ [although the second-order expression Eq. (9a) with given BCs in Eq. (9b) has a unique solution]. Then, there is a singular solution $\frac{d\bar{P}}{d\zeta} = \frac{1}{2}$ shown by the straight horizontal line (red) in Fig. 2, which separates the phase plane into two regions with solutions of different behaviors (see Sec. III B). The form of Eq. (9b) facilitates proper combinations of the integral curves and the BCs in the phase plane, as illustrated by an example in this plot. There, both BCs of Eq. (9b) are presented by the dashed line 5 for $S^+ = S^- = 0$ ($\mathcal{E}_x^2 = 1.25$). The points of intersection between this BC line and an integral curve determine the edge valley polarization $\bar{P}^{\pm}$ for samples of the thickness 2δ, i.e.,

$$2\delta = \int_{\bar{P}^-}^{\bar{P}^+}\left(\frac{d\bar{P}}{d\zeta}\right)^{-1}d\bar{P}, \tag{11}$$

where the integration is carried out along the considered integral curve. For instance, for $\bar{C} = 1$, the integration is carried out along curve 3 between points A ($\bar{P}^-$) and B ($\bar{P}^+$). For $\bar{C} = 0$, the integration along curve 2′ is similar to that of curve 3. However, for curve 2, if it is carried out from point C ($\bar{P}^-$) to $\bar{P} = 0$ or from $\bar{P} = 0$ to point D ($\bar{P}^+$), the formal integration gives $\delta \to \infty$ which corresponds to a semi-infinite sample. For $\bar{C} = -0.2$, the valley-polarization distributions presented by curves 1 and 1′ are qualitatively different in that they are characterized by the curvature of opposite signs. Indeed, for curve 1′, we have $d^2\bar{P}/d\zeta^2 > 0$ (positive curvature) while this value is negative for curve 1 (i.e., $d^2\bar{P}/d\zeta^2 < 0$; negative curvature). It is evident that the corresponding integration along the integral curves would give a finite sample thickness: $\delta_1 > \delta_{1'}$. Finally, for $\bar{C} = 2$, integral curve 4 has no intersection point with the BC line, which means the absence of solution for Eq. (9a) that is compatible with the BCs for the

chosen constant $\bar{C} = 2$. Generally, the following tendency is noted for the integral curves with increasing $\bar{C}$: an integral curve moves upward so that the intersection points (like A and B) approach to the limiting superposed position ($A \leftrightarrow B$), where both curves are tangent to one another at the maximum point ($\bar{p}_{\max} = \mathcal{E}_x^2$, $\bar{P} = 0$). Such a limiting integral curve is obtained for $\bar{C} = \bar{C}_{\max} = \bar{p}_{\max} + (1/2)\ln|2\bar{p}_{\max} - 1|$. In Fig. 2, we have $\bar{p}_{\max} = 1.3$ and $\bar{C}_{\max} = 1.5$. This limiting case corresponds to an infinitely thin sample $\delta \to 0$. For integral curves with $\bar{C} > \bar{C}_{\max}$, the above-mentioned intersection points are absent (curve 4) such that there are no solutions satisfying the imposed BCs.

III. DOMAINS OF VALLEY POLARIZATION

The expression for valley polarization $P(\zeta)$ [Eq. (8a)] is a second-order nonlinear differential equation, for which finding an exact solution in an analytically explicit form is very challenging. In developing a full physical picture on domain formation, it is therefore instructive to examine two limiting cases of *weak* ($\mathcal{E}_x \ll 1$) and *strong* ($\mathcal{E}_x \gg 1$) electric fields, where approximate analytical solutions can be obtained. Note that the solutions for these limiting cases are realized in two different regions of the phase plane mentioned above.

A. Weak electric fields

In the range of weak electric fields ($\mathcal{E}_x \ll 1$), the valley polarization is essentially different from zero only at the edges, and exponentially decays into the sample interior at the rate of the characteristic intervalley diffusion length L_{iv} [45]. The edge values of $P(\zeta)$ depend on the imposed BCs. For instance, at $S^+ = S^- = S$, we find that for $S \ll 1$ ($S \approx 0$)

$$P(\zeta) = \mathcal{E}_x \frac{\sinh\zeta}{\cosh\delta}, \tag{12a}$$

with $P(\pm\delta) = \pm\mathcal{E}_x \tanh\delta$. Alternatively, for $S \gg 1$, we obtain

$$P(\zeta) = (\mathcal{E}_x/S)\frac{\sinh\zeta}{\sinh\delta}, \tag{12b}$$

with reduced amplitudes $P(\pm\delta) = \pm\mathcal{E}_x/S$ at the edges. In the case of different S^+ and S^-, our analysis shows that if $S^+ \gg 1$ and $S^- \ll 1$, for instance, then

$$P(\zeta) = \mathcal{E}_x \frac{\sinh(\zeta - \delta)}{\cosh(2\delta)} \tag{12c}$$

with $P(\delta) = 0$ and $P(-\delta) = \mathcal{E}_x \tanh(2\delta)$.

B. Strong electric fields

When the applied electric field is much larger than the critical field E_c (i.e., $\mathcal{E}_x \gg 1$), the linear approximation fails as the nonlinear properties of Eq. (8a) become pronounced. In contrast to the case of weak fields which are characterized by the length L_{iv}, it is found that two strongly distinct length scales can now identify the regions of smooth (L_{ext}) and abrupt (L_{com}) changes in $P(\zeta)$. With $L_{\text{ext}} \gg L_{\text{com}}$, it signifies the formation of valley-polarized domains. To demonstrate this point, we simplify Eq. (8a) by considering only the first two terms which play the major role in the given condition ($\mathcal{E}_x \gg 1$) and approximately compensate each other. Thus, the equation becomes

$$\frac{d^2P}{d\zeta^2} + \mathcal{E}_x \frac{dP^2}{d\zeta} = 0. \tag{13}$$

The integration over ζ gives

$$\frac{dP}{d\zeta} + \mathcal{E}_x P^2 = \mathcal{E}_x C_1, \tag{14}$$

for which we take the constant $C_1 = C^2 > 0$ to make the case definite. The solution of Eq. (14) subsequently gives

$$P(\zeta) = C\ \tanh[C\mathcal{E}_x(\zeta - \zeta_0)], \tag{15}$$

where ζ_0 is another constant. A key feature of this solution [Eq. (15)] is that it consists of two wide regions with $P(\zeta) \approx \pm C$ (i.e., plateaus) and a narrow region of width L_{com} ($= L_{iv}/\mathcal{E}_x \propto E_x^{-1}$, the compressed intervalley diffusion length), where $P(\zeta)$ varies rapidly constituting a boundary layer between the plateaus. Thus, the formation of two oppositely valley-polarized domains separated by a domain wall is clearly identified [46]. An estimate of the third term in Eq. (8a) based on Eq. (15) shows that its contribution is indeed small in the domain wall but can play a dominant role in the plateaus.

For a more detailed analysis of the plateau regions, a different approximation of Eq. (8a) is used by dropping the second derivative of P:

$$\mathcal{E}_x \frac{dP^2}{d\zeta} - P = 0. \tag{16}$$

The corresponding solutions and appropriate BCs can be written as

$$P^{\pm}(\zeta) = \frac{\zeta - \zeta_0}{2\mathcal{E}_x} + C^{\pm}, \tag{17a}$$

$$\frac{1}{2\mathcal{E}_x} - (1 - P^{\pm 2})\mathcal{E}_x \pm S^{\pm}P^{\pm} = 0. \tag{17b}$$

Here, $C^{\pm}$ are the constants and shorthand notations $P^{\pm}(\zeta) \equiv P(\zeta \gtrless \zeta_0)$ and $P^{\pm} \equiv P(\zeta = \pm\delta)$ are adopted. The characteristic length scale for domain plateaus is termed the extended intervalley diffusion length L_{ext} ($= L_{iv}\mathcal{E}_x \propto E_x$). Using Eq. (17a), we can write

$$P^{\pm} = \frac{\pm\delta - \zeta_0}{2\mathcal{E}_x} + C^{\pm}. \tag{18}$$

On the other hand, it follows from Eq. (17b) that

$$P^{\pm} = \mp\frac{1}{2}\left[\frac{S^{\pm}}{\mathcal{E}_x} - \sqrt{\left(\frac{S^{\pm}}{\mathcal{E}_x}\right)^2 - 4\left(\frac{1}{2\mathcal{E}_x^2} - 1\right)}\right] \equiv f^{\pm}(\mathcal{E}_x, S^{\pm}). \tag{19}$$

Thus, the integration constants $C^{\pm}$ are given by

$$C^{\pm} = \frac{\zeta_0 \mp \delta}{2\mathcal{E}_x} + f^{\pm}(\mathcal{E}_x, S^{\pm}). \tag{20}$$

It then follows that for the plateaus in Eq. (17a), we obtain

$$P^{\pm}(\zeta) = \frac{\zeta \mp \delta}{2\mathcal{E}_x} + f^{\pm}(\mathcal{E}_x, S^{\pm}). \tag{21}$$

The rest of integration constants (ζ_0 and C) are determined from the condition that $P^{\pm}(\zeta)$ in Eqs. (15) and (21) are connected to each other smoothly near $\zeta \approx \zeta_0$. Then, we obtain $C = C^+ = -C^-$. Using the relationship $C^+ = -C^-$ and the fact that $C^{\pm} = P^{\pm} + (\zeta_0 \mp \delta)/2\mathcal{E}_x$ as well as Eq. (19), we find the integration constant ζ_0 as

$$\zeta_0 = -\mathcal{E}_x[f^+(\mathcal{E}_x, S^+) + f^-(\mathcal{E}_x, S^-)]. \tag{22}$$

Similarly, the integration constant C is expressed as

$$C = \frac{1}{2}\left[f^+(\mathcal{E}_x, S^+) - f^-(\mathcal{E}_x, S^-) - \frac{\delta}{\mathcal{E}_x}\right]. \tag{23}$$

Note that the expression for ζ_0 can also be readily obtained using a "step"-function distribution $P(\zeta) = \mathrm{sgn}(\zeta - \zeta_0)$ and the condition of integral balance of the carriers in each type, i.e., the valleys K and K'. The latter is equivalent to integration of Eq. (8a) over the coordinate ζ from $-\delta$ to δ, which results in

$$\zeta_0 = -\frac{1}{2}\left(\left.\frac{dP}{d\zeta}\right|_{+\delta} - \left.\frac{dP}{d\zeta}\right|_{-\delta}\right). \tag{24}$$

Taking into account the BCs [Eq. (8b)], we arrive at Eq. (22).

In the case considered ($\mathcal{E}_x \gg 1$), the obtained expressions can be further reduced to

$$\zeta_0 = \frac{S^+ - S^-}{2} - |\mathcal{E}_x|[\sqrt{1 + (S^+/2\mathcal{E}_x)^2} - \sqrt{1 + (S^-/2\mathcal{E}_x)^2}],$$

$$C = \frac{1}{2}\left[\sqrt{1 + (S^+/2\mathcal{E}_x)^2} + \sqrt{1 + (S^-/2\mathcal{E}_x)^2} - \frac{S^+ + S^-}{2\mathcal{E}_x} - \frac{\delta}{\mathcal{E}_x}\right],$$

$$P^{\pm} = \mp\left[\frac{S^{\pm}}{2\mathcal{E}_x} - \sqrt{1 + (S^{\pm}/2\mathcal{E}_x)^2}\right]. \tag{25}$$

These expressions are valid for arbitrary relationships between $S^{\pm}$ and $\mathcal{E}_x$. If the edge intervalley scattering rate is relatively low $S^{\pm}/\mathcal{E}_x \ll 1$, then

$$\zeta_0 = \frac{S^+ - S^-}{2}, \quad C = 1 - \frac{1}{2\mathcal{E}_x}\left(\delta + \frac{S^+ + S^-}{2}\right),$$

$$P^{\pm} = \pm 1 \mp \frac{S^{\pm}}{2\mathcal{E}_x} \simeq \pm 1. \tag{26}$$

Actually, different pictures can emerge depending on the relative strengths of relevant variables as discussed below.

Symmetrical case. If the intervalley scattering rates at the edges are equal, $S^+ = S^- = S$, then we obtain $\zeta_0 = 0$, $C = \sqrt{1 + (S/2\mathcal{E}_x)^2} - (S/2\mathcal{E}_x) - (\delta/2\mathcal{E}_x)$, and $P^+ = -P^- = 1 - S/2\mathcal{E}_x$. For small S ($S \ll 1$), it follows that $C = 1 - (S/2\mathcal{E}_x) - (\delta/2\mathcal{E}_x) \simeq 1$ and $P^+ = -P^- \simeq 1$. If the intervalley scattering is absent at both edges ($S = 0$), then $C = 1 - (\delta/2\mathcal{E}_x) \simeq 1$ and $P^+ = -P^- = 1$, i.e., the domains are completely polarized. In contrast, for large S ($S/\mathcal{E}_x \gg 1$), we obtain $C \simeq \mathcal{E}_x/S$ and $P^{\pm} \simeq \mathcal{E}_x/S \ll 1$ such that the valley polarization is significantly reduced. Note that the length scale characterizing the domain wall in the latter case is determined by $L_S = L_{\mathrm{com}}S/\mathcal{E}_x$, where L_{com} is the compressed intervalley diffusion length. With increasing S, the second (nonlinear) term in Eq. (8a) decreases more rapidly than the third (linear) term. Therefore, for Eq. (13) to remain valid [such that the third term in Eq. (8a) can still be dropped], the value of S must be restricted by the inequalities $\mathcal{E}_x \ll S \ll \mathcal{E}_x^2$.

Asymmetrical case. The difference between the edge scattering rates S^+ and S^- is assumed to be sufficiently large to satisfy $S^+/S^- \gg 1$ or $S^-/S^+ \gg 1$. As an example, we consider the limiting case of $S^- = 0$ and $S^+ = \infty$. Here, the valley polarization $P(\zeta)$ can be classified into the two spatial regions: a wide plateau adjacent to the edge $\zeta = -\delta$ where the intervalley scattering is absent ($S^- = 0$) and the domain wall whose slope becomes abrupt as it approaches the other edge at $\zeta = \delta$ with a high intervalley scattering ($S^+ = \infty$). Using Eqs. (17a) and (17b) for the plateau $P^-(\zeta)$ and Eqs. (15) and (8b) for the wall, we find $C = -C^-$, $C^- = -1 + \delta/\mathcal{E}_x \simeq -1$, and $\zeta_0 = \delta$. The specific dependencies of the plateau and the wall are obtained as $P^-(\zeta) = -1 + (\zeta + \delta)/2\mathcal{E}_x$ and $P^+(\zeta) = \tanh[\mathcal{E}_x(\zeta - \delta)]$, respectively, which join smoothly to each other near the edge $\zeta = \delta$. For valley polarization at the edges, we obtain, respectively, $P^- = -1$ and $P^+ = \mathcal{E}_x/S \ll 1$.

So long as both S^+ and S^- are sufficiently low (vs $\mathcal{E}_x$) even in an asymmetric case, the dependence $P = P(\zeta)$ yields two domains each covering an extensive region (domain plateaus), in which the valley polarization is almost constant and has opposite signs. As discussed earlier, the characteristic length scale for the plateaus is L_{ext} ($= L_{iv}\mathcal{E}_x \gg L_{iv}$) while the narrow region separating them (domain wall) is of the width L_{com} ($= L_{iv}/\mathcal{E}_x \ll L_{iv}$). Within the domain plateaus, the transverse field is almost constant $\mathcal{E}_y \simeq \pm a\mathcal{E}_x$; in contrast, in the domain wall, it decreases very rapidly when approaching to $\zeta = \zeta_0$ and changes its sign in accordance with Eqs. (7) and (15). As the domains of valley polarization are spatially well resolved, they contain electrons in only one of the two (K and K') valleys each. The corresponding criterion can be written as $L_{\mathrm{com}} \ll d$, which means that the domain wall is much more narrow than the sample width. This criterion requires a strong applied electric field $E_x \gg E_c' = k_BT/ae_0d$. In comparison, the previous condition $\mathcal{E}_x(= E_x/E_c) \gg 1$ can be restated as $E_x \gg (d/L_{iv})E_c'$. As such, the relative ratio d/L_{iv} determines the more stringent requirement of the two. The arrangement of domains and localization of the valley currents relative to the sample edges is associated with the direction of the external electric field. By reversing the sign of E_x, the sequential order of the domains can be switched, with the characteristic time $\sim 2d/\mu_{yx}|E_x|$, determined by leak-in of the carriers onto the sample edges.

Singular solution. Equation (8a) also has *a singular solution* of the form $P_s(\zeta) = A\zeta + B$, which can be verified by direct substitution. The integration constants are $A = 1/2\mathcal{E}_x$, $B = (1/2)[f^+(\mathcal{E}_x, S^+) + f^-(\mathcal{E}_x, S^-)]$, where $f^{\pm}(\mathcal{E}_x, S^{\pm})$ are as given in Eq. (19). The solution $P_s(\zeta)$ is realized at certain combinations in which $\mathcal{E}_x$, δ, and $S^{\pm}$ obey the equation

$$\delta = \mathcal{E}_x[f^+(\mathcal{E}_x, S^+) - f^-(\mathcal{E}_x, S^-)]. \tag{27}$$

In the parameter space, Eq. (27) gives the dimensionless thickness δ as a function of $\mathcal{E}_x$ and $S^{\pm}$. For $S^+ = S^- = S$ (symmetrical case), we obtain $B = 0$. Then, $P_s(\zeta) = \zeta/2\mathcal{E}_x$ and

$$P_s^- = -P_s^+ = \frac{1}{2}\left[\frac{S}{\mathcal{E}_x} - \sqrt{\left(\frac{S}{\mathcal{E}_x}\right)^2 + 4\left(1 - \frac{1}{2\mathcal{E}_x^2}\right)}\right]. \tag{28}$$

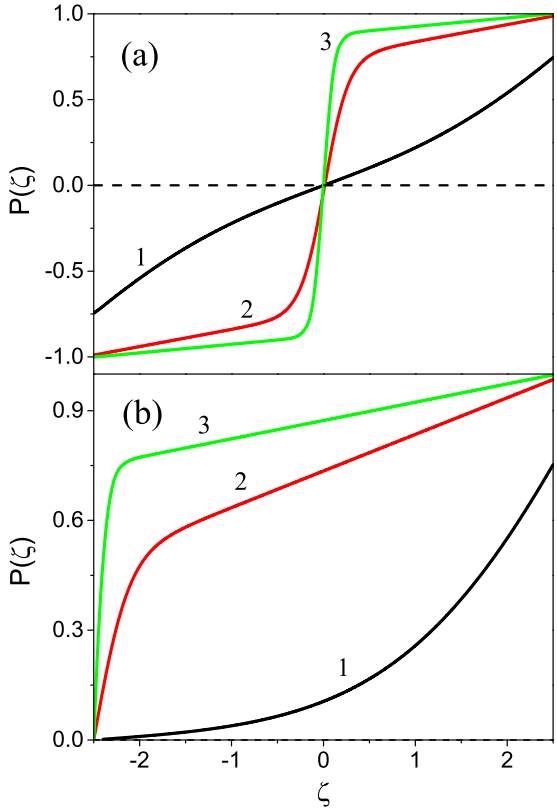

FIG. 3. Valley polarization $P(\zeta)$ calculated by numerical solution of Eqs. (8a) and (8b) for different values of $\mathcal{E}_x$ ($\delta = 2.5$). (a) $S^{\pm} = 0$ and (b) $S^{+} = 0, S^{-} = \infty$. The curves are 1 (black), $\mathcal{E}_x = 1$; 2 (red), 5; 3 (green), 10.

The relationship given in Eq. (27) takes the form

$$\delta = \left[S^2 + 2\left(2\mathcal{E}_x^2 - 1\right)\right]^{1/2} - S \tag{29}$$

or, when solved for $\mathcal{E}_x$,

$$\mathcal{E}_x = \pm\tfrac{1}{2}[\delta^2 + 2\delta S + 2]^{1/2}. \tag{30}$$

If $S = 0$, then $\mathcal{E}_x = \pm\sqrt{\delta^2 + 2}/2$ which corresponds with $\delta = 2(\mathcal{E}_x^2 - 1/2)^{1/2}$ and $P_s^{\pm} = \pm(1 - 1/2\mathcal{E}_x^2)^{1/2}$. For $S^{+} = 0$ and $S^{-} = \infty$ (asymmetrical case), on the other hand, we obtain $B = (1/2\mathcal{E}_x)(\mathcal{E}_x^2 - 1/2)^{1/2}$ and the solution becomes $P_s(\zeta) = (\zeta + \delta)/2\mathcal{E}_x$ with $P^{-} = 0$ and $P^{+} = (1 - 1/2\mathcal{E}_x^2)^{1/2}$. Here $\delta = (\mathcal{E}_x^2 - 1/2)^{1/2}$, which is by factor of 2 smaller than the case of $S^{\pm} = 0$.

An interesting point to note is that the singular solution $P_s = P_s(\zeta)$ divides the set of curves $P = P(\zeta)$ into two groups of qualitatively different behavior which may be classified by the sign of the second derivative $d^2P/d\zeta^2 \gtrless 0$ defining the curvature of a curve. The curvature of all curves has the same sign in each group, while they are oppositive between different groups. The curves $P = P(\zeta)$ of one group show a steplike behavior and form domain structure, whereas those of the other group are of the usual diffusionlike behavior.

Figure 3 shows the results for valley polarization $P(\zeta)$ obtained by numerical solution of Eqs. (8a) and (8b) using symmetric BCs $S^{+} = S^{-} = 0$ [Fig. 3(a)] and asymmetric BCs $S^{+} = 0, S^{-} = \infty$ [Fig. 3(b)] for different values of dimensionless electric field $\mathcal{E}_x$ and thickness $\delta = 2.5$. The singular solutions (not shown) are as follows: (a) $P_s(\zeta) = 0.36\zeta$ ($\mathcal{E}_x = 1.4$) and (b) $P_s(\zeta) = 0.2\zeta + 0.5$ ($\mathcal{E}_x = 2.6$).

C. Weak intervalley scattering

Weak (or completely absent) intervalley scattering in the bulk is also conducive for inhomogeneous valley polarization in the form of domains along with strong fields. Generally, this condition corresponds to a high carrier mobility and/or a long intervalley scattering time, which allows the carriers to reach the edges without intervalley scattering in the interior of the nanostructure. The appropriate criterion for such conditions reads as $2d/L_{iv} < 1$. Since d is now the primary length scale, it is convenient to redefine the dimensionless variables by replacing L_{iv} with d, i.e., $\xi = y/d$, $\mathcal{E}_x' = E_x/E_c'$, $E_c' = k_BT/(ae_0d)$, and $S'^{\pm} = 2s^{\pm}d/D$. Then, Eqs. (8a) and (8b) are expressed as

$$\frac{d^2P}{d\xi^2} + \mathcal{E}_x'\frac{dP^2}{d\xi} - \gamma^2 P = 0, \tag{31a}$$

$$\left[\frac{dP}{d\xi} - (1 - P^2)\mathcal{E}_x' \pm S'^{\pm}P\right]_{\xi=\pm1} = 0, \tag{31b}$$

where $\gamma = d/L_{iv}$. The last term in Eq. (31a) can be omitted because it contains the small parameter $\gamma^2 \ll 1$. Then, the first integration gives

$$\frac{dP}{d\xi} + \mathcal{E}_x'P^2 = C, \tag{32}$$

where the constant C is chosen as $C/\mathcal{E}_x' \equiv a_0^2$ ($E_x > 0$). The solution of Eq. (32) has the form

$$\left|\frac{P - a_0}{P + a_0}\right| = e^{-2a_0\mathcal{E}_x'(\xi - \xi_0)}, \tag{33}$$

where a_0 and ξ_0 must be found from the BCs [i.e., Eq. (31b)]. Using Eq. (32) in Eq. (31b), the latter can be written as

$$C - \mathcal{E}_x' = \mp S'^{\pm}P^{\pm}. \tag{34}$$

On the other hand, we can express the integration constants in Eq. (33) through the valley polarization $P^{\pm}$ at the edges as follows:

$$\xi_0 = \frac{1}{4\mathcal{E}_x'a_0}\ln\left|\frac{(P^{+} - a_0)(P^{-} - a_0)}{(P^{+} + a_0)(P^{-} + a_0)}\right|, \tag{35a}$$

$$a_0 = \frac{1}{4\mathcal{E}_x'}\ln\left|\frac{(P^{-} - a_0)(P^{+} + a_0)}{(P^{-} + a_0)(P^{+} - a_0)}\right|. \tag{35b}$$

Equations (33), (35a), and (35b) determine the valley polarization $P(\xi)$ for given values of $\mathcal{E}_x'$ and $S'^{\pm}$. In the following, we consider two different examples of edge intervalley scattering.

Symmetrical case. In this case, with $S'^{+} = S'^{-} = 0$, it follows from Eqs. (31a) and (31b) that the solution $P(\xi)$ is an odd function of ξ, and the edge polarization is equal to $P^{+} = -P^{-} = \tanh(\mathcal{E}_x')$. We find that $C = \mathcal{E}_x'$, $\xi_0 = 0$, $a_0 = 1$, and the valley polarization is given by

$$P(\xi) = \tanh(\mathcal{E}_x'\xi). \tag{36}$$

It is seen that the thickness of the domain wall is of the order of $L_{\text{com}} = k_BT/ae_0E_x \propto E_x^{-1}$, i.e., inversely proportional to the field E_x. For strong fields $E_x \gg E_c'$ ($= k_BT/ae_0d$), the domain

wall thickness is much narrower than the sample width $2d$. Out of this narrow region, the valley polarization rapidly saturates $|P(\xi)| \simeq \tanh(\mathcal{E}'_x) \simeq 1$, and the regions of domain plateau are formed where the carriers of only one valley are present exclusively.

Asymmetrical case. Here, we assume the difference in the edge intervalley scattering rates to be large, which can be described by the theoretical limit of zero and infinite values, for example, as $S'^{+} = 0$ and $S'^{-} = \infty$. Then, we find $P^{-} = 0$, $P^{+} = \tanh(2\mathcal{E}'_x) \simeq 1$, and $\xi_0 = -1$. The valley polarization is given by $P(\xi) = \tanh[\mathcal{E}'_x(\xi + 1)]$. In this case, the carriers of only one valley (K) are distributed across the whole width of the sample, except a narrow region near the edge $\xi = -1$, where a strong edge intervalley scattering mixes effectively the carriers in the two valleys.

D. Nonlinear current

Taking into account the symmetry properties of the kinetic coefficients and using dimensionless variables, the valley current densities $J_x^{K,K'} = -e_0 i_x^{K,K'}/j_c$ can be obtained as

$$J_x^K(\zeta) = \frac{1}{2}\left[(1+P)\mathcal{E}_x + a^2 P(1+P)\mathcal{E}_x + a^2\frac{dP}{d\zeta}\right],$$
$$J_x^{K'}(\zeta) = \frac{1}{2}\left[(1-P)\mathcal{E}_x - a^2 P(1-P)\mathcal{E}_x + a^2\frac{dP}{d\zeta}\right]. \quad (37)$$

Here, we utilize the relationships $\mathcal{E}_y(\zeta) = aP(\zeta)\mathcal{E}_x$, $n_K = (1+P)N/2$, $n_{K'} = (1-P)N/2$, and $j_c = e_0\mu_{yy}^K N E_c$. The total longitudinal current density $J_x(\zeta) = J_x^K(\zeta) + J_x^{K'}(\zeta)$ is

$$J_x(\zeta) = \mathcal{E}_x + a^2 P^2(\zeta)\mathcal{E}_x + a^2\frac{dP}{d\zeta}, \quad (38)$$

where the last two terms contain the anisotropy parameter (i.e., a) associated with the Berry curvature and anomalous transport. More specifically, the second term is proportional to the transverse electric field $\mathcal{E}_y$, and the last term is due to carrier diffusion.

Figures 4 and 5 provide the transverse distributions of the current densities, obtained by Eqs. (37) and (38) (also see Sec. II of Supplemental Material [45]), for the valley polarization shown in Fig. 3 by curves 2 (red) for different BCs: (a) $S^{\pm} = 0$ and (b) $S^{+} = 0, S^{-} = \infty$. The upper panel presents the longitudinal valley current densities $J_x^K(\zeta)$ and $J_x^{K'}(\zeta)$ along with the total current density $J_x(\zeta) = J_x^K(\zeta) + J_x^{K'}(\zeta)$. In comparison, the lower panel shows the vector field of the valley current densities $\mathbf{J}^K$ and $\mathbf{J}^{K'}$. The direction of the arrows is defined by the angle $\varphi_{K(K')}$ [i.e., $\tan(\varphi_{K(K')}) = J_y^{K(K')}/J_x^{K(K')}$], while the arrow length shows the total valley current density $\mathbf{J}^{K(K')} = J_x^{K(K')}\hat{\mathbf{i}} + J_y^{K(K')}\hat{\mathbf{j}}$.

Since $P(\zeta)$ depends on $\mathcal{E}_x$, the current density $J_x = J_x(\mathcal{E}_x)$ may have regions of nonlinear behavior as a function of $\mathcal{E}_x$. The last two terms in Eq. (38) are positive ($\mathcal{E}_x > 0$) and result in an increase of J_x in addition to the first (Ohmic) term. Such a peculiar feature of anomalous transport enhancing the longitudinal carrier motion is inherent in the Berry curvature as reported earlier [20]. Hence, a superlinear dependence in the current-voltage (I-V) characteristic $J_x = J_x(\mathcal{E}_x)$ may be observed in the field range where the valley polarization domains are formed. Integrating Eq. (38) over y, we obtain the

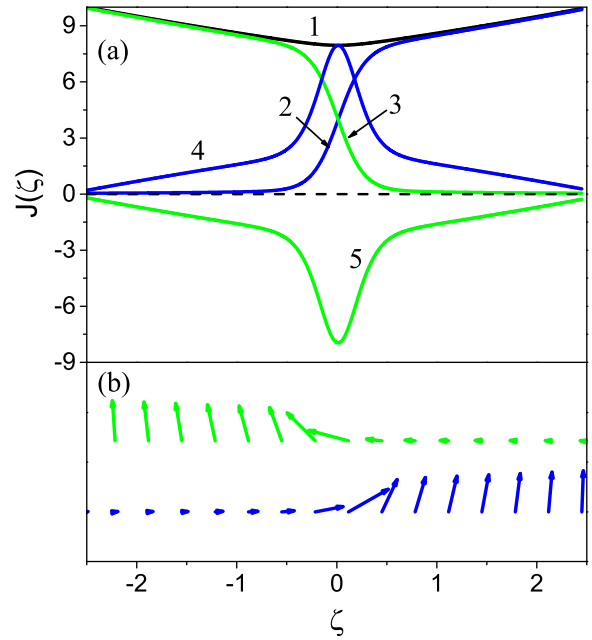

FIG. 4. Transverse distributions of dimensionless current densities calculated using the valley polarization of curve 2 (red) in Fig. 3(a) ($S^{\pm} = 0; \mathcal{E}_x = 5, \delta = 2.5$). (a) Line 1 (black) is the total longitudinal current density $J_x = J_x^K + J_x^{K'}$; lines 2 (blue) and 3 (green) are for J_x^K and $J_x^{K'}$, respectively. Lines 4 (blue) and 5 (green) are for J_y^K and $J_y^{K'}$, respectively. (b) An arbitrary-scale map of vector field given by the valley current densities $\mathbf{J}^K$ (blue) and $\mathbf{J}^{K'}$ (green). The direction of arrows is defined by angle $\varphi_{K(K')}$, where $\tan(\varphi_{K(K')}) = J_y^{K(K')}/J_x^{K(K')}$, and the arrow length is defined by total valley current density $\mathbf{J}^{K(K')} = J_x^{K(K')}\hat{\mathbf{i}} + J_y^{K(K')}\hat{\mathbf{j}}$.

total current through the sample

$$I_x = e_0 N D\left\{a[P(\delta) - P(-\delta)] + \frac{e_0 L_{iv}}{k_B T}E_x\int_{-\delta}^{\delta}(1 + a^2P^2)d\zeta\right\}. \quad (39)$$

To elucidate the expected nonlinear change in the I-V characteristics caused by the domains' formation with increasing E_x, two cases of weak and strong electric fields E_x are compared below.

For weak fields ($\mathcal{E}_x \ll 1$), we obtain from Eq. (39) in the linear approximation

$$I_x = 2d\sigma[1 + a^2 g(\delta, S^{\pm})]E_x \equiv 2d\,\Xi_0 E_x, \quad (40)$$

where $\sigma = e_0\mu N$, Ξ_0 is the electrical conductivity in the linear regime, and g is given as [see also Eq. (2b) of Supplemental Material [45]]

$$g(\delta, S^{\pm}) = \frac{[2\,\sinh(\delta) + (S^{+} + S^{-})\cosh(\delta)]\sinh(\delta)}{[(1 + S^{+}S^{-})\sinh(2\delta) + (S^{+} + S^{-})\cosh(2\delta)]\delta}. \quad (41)$$

In a wide sample ($\delta \gg 1$), the electrons of different valleys are collected mostly in the vicinity of opposite edges ($\zeta = \pm\delta$). In this case, we obtain

$$g(\delta, S^{\pm}) = \frac{1 + (S^{+} + S^{-})/2}{(1 + S^{+} + S^{-} + S^{+}S^{-})\delta}. \quad (42)$$

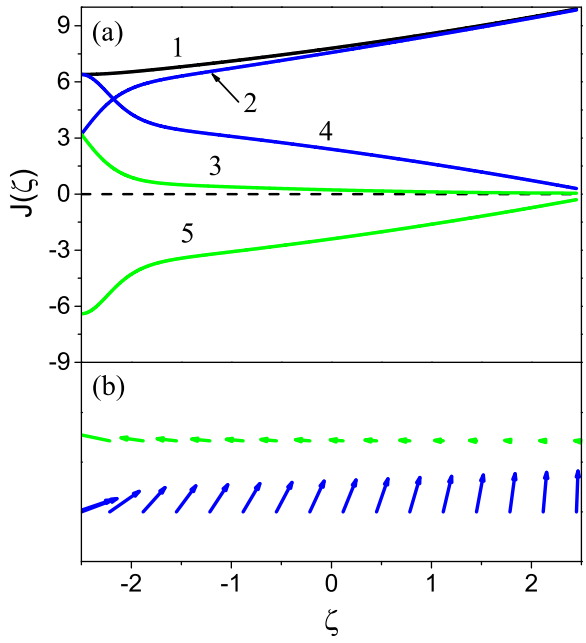

FIG. 5. Transverse distributions of dimensionless current densities calculated using the valley polarization of curve 2 (red) in Fig. 3(b) ($S^+ = 0, S^- = \infty; \mathcal{E}_x = 5, \delta = 2.5$). (a) Line 1 (black) is the total longitudinal current density $J_x = J_x^K + J_x^{K'}$; lines 2 (blue) and 3 (green) are for J_x^K and $J_x^{K'}$, respectively. Lines 4 (blue) and 5 (green) are for J_y^K and $J_y^{K'}$, respectively. (b) Vector field map given by the valley current densities $\mathbf{J}^K$ (blue) and $\mathbf{J}^{K'}$ (green).

If $S^+ = S^- = S$, then $g = 1/(1+S)\delta$ and Ξ_0 becomes $\Xi_0 = \sigma[1 + a^2/(1+S)\delta]$. In a narrow sample ($\delta \ll 1$), it follows that $g = 1$ independent of $S^\pm$, and $\Xi_0 = \sigma(1+a^2)$. For intermediate values of δ (in particular, for $\delta \sim 1$), we find that if $S^+ = S^- = 0$, then $g = \tanh\delta/\delta$ and $\Xi_0 = \sigma[1 + a^2 \tanh\delta/\delta]$. For $S \gg 1$ ($S \to \infty$), we obtain $g = 1/\delta S$ and $\Xi_0 = \sigma(1 + a^2/\delta S)$ (here, if $\delta \ll 1$, we assume that $S\delta \gg 1$). If the intervalley scattering rates at the edges are different, for example, $S^+ = \infty$ and $S^- = 0$, we find that $g = \tanh(2\delta)/2\delta$ and $\Xi_0 = \sigma[1 + a^2 \tanh(2\delta)/2\delta]$.

For strong fields ($\mathcal{E}_x \gg 1$), when the valley-polarization domains are formed, we obtain from Eq. (39) the I-V characteristics of the form

$$I_x = 2d\sigma(1+a^2)E_x + I_x^0, \tag{43}$$

where I_x^0 is given by

$$I_x^0 = 2e_0 NDa\left[1 + \tfrac{1}{2}\left(\zeta_0^2 - \delta^2 - \delta(S^+ + S^-)\right)\right] \tag{44}$$

if ζ_0 of Eq. (26) is not too close to one of the edges; and

$$I_x^0 = e_0 NDa(1 - 2\delta^2) \tag{45}$$

if $|\zeta_0| \simeq \delta$.

To demonstrate the nonlinear I-V characteristics, we consider an example with $S^\pm = 0$, then $\zeta_0 = 0$ and $g(\delta) = \tanh\delta/\delta$ [Eqs. (26) and (41), respectively]. For weak fields, we obtain $I_x = 2d\sigma[1 + a^2 \tanh(\delta)/\delta]E_x$. In contrast, the current I_x for a strong field is given by Eq. (43) with $I_x^0 = 2e_0 NDa(1 - \delta^2/2)$. It is evident from the comparison that the I-V relation is nonlinear in the region transitioning from weak to strong electric fields. The effective electrical conductivity Ξ_0 in the weak fields depends on δ and is smaller than its strong-field counterpart $\Xi_\infty = \sigma(1+a^2)$ by a factor of $[1 + a^2 \tanh(\delta)/\delta]/(1+a^2)$. The parameter I_x^0 also depends on δ and changes the sign with increasing δ (from positive to negative values) at $\delta = \delta_c = \sqrt{2}$. For asymmetric BCs (for instance, $S^+ = \infty, S^- = 0$), the I-V characteristics show the similar qualitative behavior, where the I_x^0 of Eq. (45) changes the sign at $\delta = \delta_c = \sqrt{2}/2$.

In the limit of *weak intervalley scattering* ($\tau_{iv} \to \infty$), the I-V characteristics can be obtained using Eqs. (37) and (38), where d is used to normalize dimensionless parameters in place of L_{iv}. Then, we obtain

$$J_x^{K,K'}(\xi) = \tfrac{1}{2}(1+a^2)[1 \pm P(\xi)]\mathcal{E}_x', \tag{46}$$

where the relationship $\mathcal{E}_x' P^2 + dP/d\xi = \mathcal{E}_x'$ is used. By integrating the total current density $J_x = J_x^K(\xi) + J_x^{K'}(\xi) = (1 + a^2)\mathcal{E}_x'$, we find

$$I_x = 2d\sigma(1+a^2)E_x. \tag{47}$$

An identical result can be obtained from Eq. (39) if the valley polarization $P(\xi)$ given in Eq. (36) is used. Note that the I-V relation [Eq. (47)] is linear within the entire field region considered. This observation can be qualitatively understood as follows. For weak intervalley scattering, in particular, in the limit of $\tau_{iv} \to \infty$, the intervalley diffusion length $L_{iv} \to \infty$ as well. Consequently, the characteristic electric field E_c that determines the range of strong fields $E_x \gg E_c$ goes to zero, allowing E_x of any strength to meet the strong-field criterion and the linear I-V dependence throughout the range. Nevertheless, the valley-contrasting domains with the domain wall much narrower than the sample width are formed only under the criterion $E_x \gg E_c' = k_B T/ae_0 d$ (Sec. III C).

E. Control of domains with transverse current

An ansatz alternative to the condition of $i_y = 0$ is a constant nonzero transverse flux (or current), which can be imposed with an external circuit. In this case, the BCs [Eq. (6)] may depend explicitly on the specific properties of the edges, Hall-type contacts, and the external circuit (for instance, the selectivity of the valley currents, etc.). We assume that the electrical contact to the right edge of a sample is an anode and the left one is a cathode. This choice of the anode or cathode does not result in the loss of generality in our consideration, while leading to a specific asymmetry in that the carrier flux (current) densities now have definite signs "+" ($i_y > 0$) and "−" ($j_y = -e_0 i_y < 0$), respectively (Fig. 1).

Below, we use the theoretical procedure described in Sec. III B [45]. The domain plateaus are given by

$$P^\pm(\zeta) = \frac{\zeta \mp \delta}{2\mathcal{E}_x} + f^\pm(\mathcal{E}_x, S_c^\pm), \tag{48}$$

and the domain wall is expressed as

$$P(\zeta) = C\ \tanh[C\mathcal{E}_x(\zeta - \zeta_0)] - \frac{J_y}{2a\mathcal{E}_x}, \tag{49}$$

where J_y is the dimensionless transverse current density as defined earlier and the integration constant C is

$$C = \frac{1}{2}\left[f^+(\mathcal{E}_x, S_c^+) - f^-(\mathcal{E}_x, S_c^-) - \frac{\delta}{\mathcal{E}_x}\right]. \tag{50}$$

The position of the domain wall is now dependent on J_y as

$$\zeta_0 = -\mathcal{E}_x[f^+(\mathcal{E}_x, S_c^+) + f^-(\mathcal{E}_x, S_c^-)] - \frac{J_y}{a}. \tag{51}$$

Here $f^{\pm}(\mathcal{E}_x, S_c^{\pm})$ are given in Eq. (19) with the replacement of $S^{\pm}$ by $S_e^{\pm}$, where $S_e^+ = S^+$ and $S_e^- = S^- - J_y/a$ are effective intervalley scattering rates at the edges $\zeta = \pm\delta$ modified by the given J_y. For strong fields $\mathcal{E}_x$ and finite $S^{\pm}$ $[(S^{\pm}/\mathcal{E}_x)^2 \ll 1]$, we obtain

$$\zeta_0 = \frac{1}{2}\left(S^+ - S^- - \frac{1}{a}J_y\right), \tag{52}$$

which is the analog of ζ_0 in Eq. (25) for the case of $J_y \neq 0$. As it can be seen from the comparison of Eqs. (25) and (52), the position of the domain wall ζ_0 is shifted to one of the edges, where the direction of the shift $\delta\zeta = -J_y/2a$ is determined by the polarity of J_y. In a dimensional form, it is given by

$$\delta y = L_{iv}\delta\zeta = -j_y\tau/4e_0N. \tag{53}$$

The shift increases with the increasing value of $|j_y|$; the wall can reach one of the edges at $|j_y| = 4e_0Nd/\tau = e_0(2d)N/(\tau/2)$. In this case, the domain formation is associated with only one valley (K or K'). The potential difference $U = \varphi_a - \varphi_c$ (i.e., voltage drop across the sample width) can be calculated as $U = \int_{-\delta}^{\delta}(d\varphi/d\zeta)d\zeta = -\int_{-\delta}^{\delta}\mathcal{E}_y(\zeta)d\zeta$. As $\mathcal{E}_y(\zeta)$ is given in terms of $\mathcal{E}_x$, J_y, and P [45], we can obtain

$$U = -(2\delta + \mathcal{E}_x)J_y. \tag{54}$$

IV. BEYOND THE QUASINEUTRALITY CONDITION

The formation of domains with drastic redistribution of carriers between the two inequivalent valleys K and K' can be accompanied by a violation of the quasineutrality condition [Eq. (3)]. Indeed, in the domain wall as well as at the sample edges where the electric field $E_y(y)$ can vary rapidly, one may expect accumulation of electric charges such that the condition given in Eq. (3) may not be obeyed. The electric field $\mathbf{E}^i = (E_y^i, E_z^i)$, corresponding to the induced electric charge density $\varrho(y) = e_0[N - n(y)]$, is determined by the Poisson equation $\nabla \cdot E^i(y,z) = -\nabla^2\phi = (4\pi/\varepsilon_0)\varrho(y)\delta(z)$, where $n(y) = n_K(y) + n_{K'}(y)$ is the local carrier density, $\phi = \phi(y,z)$ is the electrostatic potential, ε_0 is the dielectric constant, and $\delta(z)$ is the delta function. Using the 2D Green function [47], the electrostatic potential in the given geometry ($d_x \gg d_y, d_z$) can be expressed in the standard form [48] as

$$\Phi(Y,Z) = -\frac{d_y}{4\pi L_D}\int_{-1/2}^{1/2}\delta\kappa(Y')\ln[(Y-Y')^2 + Z^2]dY'. \tag{55}$$

Here, $\Phi = e_0\phi/k_BT$, $Y = y/d_y$, $Z = z/d_y$, $\kappa(Y) = n(Y)/N$, $\delta\kappa(Y) = 1 - \kappa(Y)$, and $L_D = \varepsilon_0 k_BT/4\pi e_0^2N$ is the screening length. From Eq. (55), the transverse components of electric field $\mathcal{E}_y^i = -(aL_{iv}/2\pi L_D)\partial\Phi(Y,Z)/\partial Y$ and $\mathcal{E}_z^i = -(aL_{iv}/2\pi L_D)\partial\Phi(Y,Z)/\partial Z$ can be readily obtained. In particular, the in-plane electric field $\mathcal{E}_y^i(Y) = \mathcal{E}_y^i(Y, Z=0)$ is given by

$$\mathcal{E}_y^i(Y) = \frac{aL_{iv}}{2\pi L_D}\int_{-1/2}^{1/2}\frac{\delta\kappa(Y')}{Y-Y'}dY'. \tag{56}$$

For an accurate solution, the above equations need to be integrated self-consistently in combination with transport equations as in Refs. [49,50], where a self-consistent electrostatic problem was considered for the space-charge limited 2D transport. Instead, for our purpose here, it is possible to exploit a simplified iterative procedure based on the small aspect ratio $L_D/d_y \ll 1$ [Eq. (55)]. Using the expressions for transverse electric field given in Eqs. (56) and (7) in the condition $\mathcal{E}_y^i(Y, Z=0) = \mathcal{E}_y(Y)$, we can arrive at an integral equation for the induced electric charge $\delta\kappa(Y)$:

$$\int_{-1/2}^{1/2}\frac{\delta\kappa(Y')}{Y-Y'}dY' = 2\pi\frac{L_D}{L_{iv}}\mathcal{E}_xP(Y), \tag{57}$$

where $P(Y)$ is the solution of quasineutral problem obtained in Sec. III.

Equation (57) refers to the class of singular integral equations of the first kind with kernel of the Cauchy type and a finite integration interval in the real axis, where the integral is understood in the principal sense [51]. Its solution, bounded at both ends $Y = \pm\frac{1}{2}$, can be written as

$$\delta\kappa(Y) = \frac{2L_D}{\pi L_{iv}}\mathcal{E}_x\left(\frac{1}{4} - Y^2\right)^{1/2}\int_{-1/2}^{1/2}\frac{P(t)dt}{(t-Y)\left(\frac{1}{4}-t^2\right)^{1/2}}. \tag{58}$$

Note that for an odd function $P(Y)$ the solution $\delta\kappa(Y)$ is an even function $\delta\kappa(Y) = \delta\kappa(-Y)$. The electric charge distribution has a maximum $\delta\kappa_m$ at $Y = 0$, which can be calculated as

$$\delta\kappa_m = \frac{2L_D}{\pi L_{iv}}\mathcal{E}_x\int_0^{1/2}\frac{P(t)dt}{t\left(\frac{1}{4}-t^2\right)^{1/2}}. \tag{59}$$

In Fig. 6, we show the excess electric charge distributions $\varrho(\zeta) = e_0N\delta\kappa(\zeta)$ calculated from Eq. (58) using the valley polarization $P(\zeta)$ presented in Fig. 3(a). For ease of presentation, the results are normalized to $\varrho_0 = 2e_0NL_D\mathcal{E}_x/\pi L_{iv}$. In addition, curves 2 and 3 are scaled with the reduction factors of 0.2 and 0.1, respectively (noted above the curves). For the symmetric BCs used in the calculations ($S^{\pm} = 0$), the charge distributions indicate a maximum at the central point $\zeta = 0$. These maxima are formed due to the removal of electrons by the electric field to the sample edges, and become sharper with the increasing $\mathcal{E}_x$ that coincides with the formation of domains.

The induced electric charge density $\delta\kappa(Y)$ characterizes the extent of deviation from local quasineutrality $\kappa(Y) = 1$. The calculations show that the correction $\delta\kappa \sim L_D/L_{iv}$ is small in proportion to the smallness of the ratio $L_D/L_{iv} \ll 1$. If $\delta\kappa(Y)$ is obtained for a given value of $\mathcal{E}_x$, then the electrostatic potential $\Phi = \Phi(Y,Z)$ and transverse electric field $\{\mathcal{E}_y^i(Y,Z), \mathcal{E}_z^i(Y,Z)\}$ can be calculated by the substitution of $\delta\kappa(Y)$ in Eq. (55). Since the electrons of the K and K' valleys are displaced by the field toward the opposite edges, a net positive charge $[\delta\kappa(Y) > 0]$ develops in the interior of

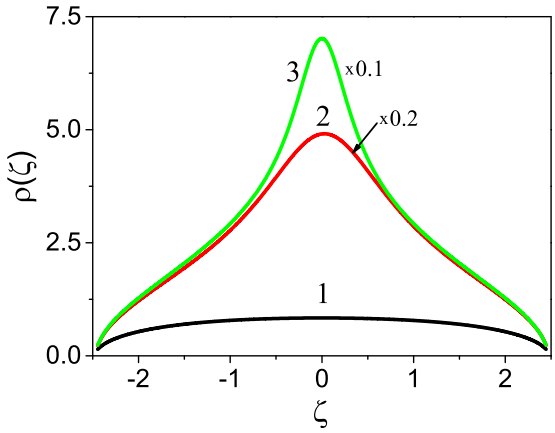

FIG. 6. Normalized electric charge density $\varrho(\zeta)/\varrho_0$ $[= e_0 N \delta\kappa(\zeta)/2e_0 N L_D \mathcal{E}_x \pi^{-1} L_{iv}^{-1}]$ calculated for three different values of dimensionless field, i.e., $\mathcal{E}_x = 1$ (curve 1, black), $\mathcal{E}_x = 5$ (curve 2, red), and $\mathcal{E}_x = 10$ (curve 3, green). The heights of curves 2 and 3 are reduced by a factor of 0.2 and 0.1, respectively, for ease of presentation. In all three cases, $S^{\pm} = 0$ and $\delta = 2.5$ are assumed.

the nanostructure. Needless to say, the net positive charge in the bulk (i.e., interior) is fully compensated by the negative charges (i.e., electrons) accumulated at the edges to maintain the overall charge neutrality. An approximate analytical evaluation for $\delta\kappa$ in each region can be found in Ref. [45].

V. DISCUSSIONS

The theory of valley-polarization domains based on the notion of valley-contrasting topological currents, developed in the preceding sections, contains several parameters: the carrier mobility μ (diffusion coefficient D), the intervalley scattering time τ, the intervalley diffusion length L_{iv}, and the characteristic diffusion field E_c; the latter separates the ranges of weak ($E_x \ll E_c$) and strong ($E_x \gg E_c$) electric fields. The two different types of spatial distributions of valley polarization $P(y)$ are realized in a sample of finite thickness, depending on the strength of the external field E_x. In the range of weak fields, a population difference in the two valleys is created only in direct vicinity of the opposite edges and rapidly decays into the interior of a sample on the characteristic length L_{iv}, typical for linear theory. In contrast, for strong fields, the nonlinear domain structure is formed under which the sample splits into two spatial domains of contrasting valley polarization with $|P| \sim 1$. At that, the two different length scales determine the extent of the domain plateau $L_{\rm ext} = L_{iv} E_x/E_c$ and the domain wall $L_{\rm com} = L_{iv} E_c/E_x$, with the contrast ratio $C_{\rm cr} = L_{\rm ext}/L_{\rm com} = E_x^2/E_c^2$.

Recent progress in the technology of growth and isolation of various 2D crystals has facilitated the discovery of a large variety of electronic systems which energy bands possess a nonzero, valley-contrasting Bloch-band Berry curvature [38]. Among them, examples of most interest are presented by two groups of semiconductor materials with broken spatial inversion symmetry, where the VHE has been studied by theory and experiments [19,20]. These include the following: (i) gapped Dirac semiconductors [graphene placed on top of hexagonal boron nitride (G/hBN)] [13,39], biased bilayer graphene (BLG) nanostructures [12]; and (ii) hexagonal monolayer group-VI TMDs [1,15,18,20,40]. The former features a relatively high carrier mobility $\mu \sim$ several units $\times(10^3 \ldots 10^4)$ cm^2/Vs, while for the latter it is much lower $\mu \sim (1 \ldots 10^3)$ cm^2/Vs. Within each of the groups, a wide spreading in the experimental data is observed for the mobility and intervalley scattering time, depending on the material and heterostructure quality and temperature.

For numerical estimations, we consider two examples of n-doped 2D honeycomb lattice systems, exhibiting topological valley transport and VHE ($a \sim 1$), which can be classified by high ($\mu = \mu_h$) and low ($\mu = \mu_l$) electron mobilities. The former is represented by graphene-based G/hBN and BLG, and the latter by monolayer TMDs. Specifically, for order-of-magnitude estimations, we take $\mu_h = 5 \times 10^4$ cm^2/Vs [12,13] and $\mu_l = 10$ cm^2/Vs [19], respectively. The rest of the kinetic coefficients and parameters relevant to the developed theoretical model are chosen as follows:

(i) In the first example, we take for the intervalley scattering time $\tau = 50$ ps, the diffusion coefficient $D = 330$ cm^2/s ($T = 77$ K). Then, we estimate the valley diffusion length $L_{iv} = 0.9$ μm and the electric field $E_c = 70$ V/cm. For example, if the applied external voltage creates the electric field $E = 5E_c = 350$ V/cm ($\mathcal{E} = 5$, Figs. 3–6), then the domain plateau and the wall scales are estimated as $L_{\rm ext} \simeq 5$ μm and $L_{\rm com} \simeq 0.2$ μm, with the domain contrast ratio $C_{\rm cr} = 25$. We note that by reversing the applied external electric field, the valley polarization and the localization of valley currents is abruptly switchable. The characteristic switching time is determined by the ratio $2d/\mu_{yx}|E_x|$. Using the above-mentioned parameters and setting $d = 5$ μm, the estimation suggests switching time of the order of $\approx 6 \times 10^{-11}$ s.

(ii) In the second example, we use the data obtained for an n-type MoS_2 field-effect transistor channel, where the electron mobility $\sim$10 cm^2/Vs and the intervalley scattering length $\sim$0.6 μm have been extracted from the measurements at room temperature [19]. With these data, we estimate the electron diffusion coefficient $D \simeq 0.3$ cm^2/s and thereby the intervalley scattering time $\tau \simeq 30$ ns. Note that ultralong intervalley scattering lifetimes (>10 ns) have also been observed in monolayer WSe_2 and WSe_2/MoS_2 heterostructures [52,53]. The characteristic critical field is estimated to be $E_c =$ 0.4 kV/cm. For the electron transport, the external voltage $V_{ds} = 5$ V applied across the distance of 5 μm creates the average driving field $E_x = 10$ kV/cm, which corresponds to a strong-field regime ($\mathcal{E} = E_x/E_c = 25 \gg 1$). The characteristic length scales for the domain plateau and the wall are estimated as $L_{\rm ext} \simeq 15$ μm and $L_{\rm com} \simeq 2.5 \times 10^{-2}$ μm, with the domain contrast ratio $C_{\rm cr} \simeq 6 \times 10^2$. Also, the intervalley scattering rates at the edges can be estimated as $s = 2 \times 10^3$ cm/s ($S = 1$).

The calculations show that if the intervalley scattering at the edges is considerable ($S > 1$), it can reduce intervalley polarization near the edges, even though it is weak or completely absent in the sample interior. Actually, strong inequalities $S \ll 1$ and $S \gg 1$ can be treated as theoretical limits $S \to 0$ and $S \to \infty$, respectively. The intervalley scattering rate is known to depend on the type of edges (zigzag, arm-

chair). The conducting channels with zigzag edges promote to avoid such effect since in this case the intervalley scattering at the edges is suppressed [54,55]. Also, in semiconductors with a finite-energy band gap, lateral confinement potential imposed by electrostatic gating can form potential barriers for the electrons moving to the edges, thereby excluding (or considerably reducing) their edge intervalley scattering rates.

We have estimated the induced electric charge density due to possible deviation from the local quasi-neutrality condition used in the theory. The estimated correction has been shown to be small in proportion to the smallness of the ratio $L_D/L_{iv} \ll 1$, where L_D is the characteristic screening length.

The considered transverse valley-polarized domains can be referred to a wide class of anisotropic size effects, which have been studied a long time ago in bulklike semiconductors [37,56]. At the present time, it is noted a growing interest for revisiting the subject [57–59] through the use of modern low-dimensional (2D) electronic systems as well as the availability of different experimental methods. Experimental verification of the predicted valley-polarized domains controlled by the applied electric field can be done by utilizing the existing methodologies focused on the spatial dependence of optical properties in the considered materials: polarization-resolved photoluminescence spectroscopy, time-resolved Kerr rotation microscopy [60], Kelvin probe force microscopy which enables nanometer-scale imaging of the surface potential [61]. Let us enumerate some of the transport and optical properties which can evidence for the domain formation. Indeed, the studied domains can manifest themselves by the spatially separated valley currents; reconstruction of the local potential distributions associated with the domain structure; and as response to a transverse current and polarization-resolved optical excitation.

If the electron mean-free path is long enough, semiconductor devices of restricted geometry tend to operate in the ballistic or quasiballistic regime. In this case, the valley-polarized domains also can be induced by a strong electric field. However, the theoretical analysis should be carried out on the base of the Boltzmann kinetic equation for the electron distribution function similarly to the classical size effects [37]. The electron momentum and intervalley scattering at the edges can impact the longitudinal transport characteristics via the combination of size effects determined by both kinds of the edge scattering [37,59].

The intrinsic valley-contrasting mechanism enters drift-diffusion equations via the carrier transport anisotropy described by valley-dependent mobilities and diffusivities. These kinetic coefficients can be calculated by integration of the Berry curvature with the carrier distribution function over the momentum space, with taking into account details of the Berry curvature distribution around the K and K' valleys [20,35,36,38,43,62,63]. Thereby, the developed model establishes its applicability for describing the valley-polarized domains formation via alternative (extrinsic) mechanisms which may play a similar role, such as strain [62] or asymmetric scattering by impurities and defects [38,63].

In the theoretical analysis presented in this work, we disregarded, for simplicity, the effect of spin-orbit coupling, which is known to be strong in monolayer TMDs and can result in a sizable spin splitting of different valleys in both the conduction ($\sim$3 . . . 50 meV) and the valence ($\sim$150 . . . 480 meV) bands [64]. Hence, for the conditions necessary for population only the lowest spin subbands may be achieved. As a consequence, spin-valley-polarized domains controlled by an external electric field can be formed. In this case, the population difference in the two valleys of such spin-valley domains may be detected through a magnetic signal from valley orbital and spin magnetic moments [38,39].

Recently, it has been demonstrated experimentally [16] that a homogeneous valley magnetization can be electrically induced from the valley magnetoelectric effect in a strained monolayer MoS_2. The valley magnetic domain formation has been studied resulting from the net Berry curvature imbalance in strained and biased electron-doped monolayer MoS_2 [35] and bilayer MoS_2 under a vertical electric field [36]. The effective electric field, which direction is perpendicular to the bias field and imposed by the strain, can be estimated as tens of V/cm [35]. For the valley-polarized domains considered in this work, the induced transverse electric field is of the order of the applied external field $\sim 10^3$ V/cm, and it has an opposite orientation in the two domains. This suggests that one can expect the formation of two magnetic domains with opposite magnetization.

As a final remark, we would like to note that the valley Hall effect has been observed experimentally using Hall bar device configurations [13,15], where the driving current flows along the shortest device dimension so that the geometry aspect ratio $r = \text{length/width} \lesssim 1$, or even much less than unity. Conversely, the sample geometry considered in this paper (most optimal for an experiment) rather corresponds to the inverse aspect ratio $r \gg 1$.

VI. SUMMARY

In this work, we have demonstrated that the valley Hall effect in 2D conducting channels of finite width $\sim L_{iv}$ (L_{iv} is the intervalley diffusion length) made of Dirac-type honeycomb semiconductors can result in the formation of valley-polarized domains, which are spatially well resolved and thereby allow the valley degree of freedom to be accessed independently. The domains appear in the transverse direction relative to the applied electric field at the field strength $E \gg E_c$, where E_c is the characteristic diffusion field. They are characterized by extensive plateaus of the order of $L_{\text{ext}} = L_{iv}E/E_c$ and a narrow wall of the order of $L_{\text{com}} = L_{iv}E_c/E$. Within each of the domains, the carriers are fully valley polarized which enables a pure bulk valley current inside the considered domain region. The current-voltage characteristic shows the superlinear behavior in the range of electric fields corresponding to the domain formation; the latter is a distinctive feature of the anomalous transport which enhances the longitudinal carrier motion.

We have investigated the behavior of the domains in different physical regimes and shown that the position of the domain wall depends on the boundary conditions at the edges. The central position of the wall (i.e., in the middle of the

sample width) is realized at the symmetrical boundary conditions, in particular, at zero intervalley scattering rate at the edges. Moreover, its position can be controlled with a transverse current flowing across the sample between the edge contacts.

We hope that this work could suggest an unexplored possibility of using the sharp spatial separation of valley carriers in the form of domains across 2D conducting channels induced and controlled by an external electric field for both valley-related physics and valleytronics applications.

ACKNOWLEDGMENT

K.W.K. acknowledges the support of the U.S. Army Research Office under a Grant No. W911NF-16-1-0472.

[1] J. R. Schaibley, H. Yu, G. Clark, P. Rivera, J. S. Ross, K. L. Seyler, W. Yao, and X. Xu, Nat. Rev. Mater. **1**, 16055 (2016).

[2] S. A. Vitale, D. Nezich, J. O. Varghese, P. Kim, N. Gedik, P. Jarillo-Herrero, D. Xiao, and M. Rothschild, Small **14**, 1801483 (2018).

[3] W. Yao, D. Xiao, and Q. Niu, Phys. Rev. B **77**, 235406 (2008).

[4] O. Gunawan, Y. P. Shkolnikov, K. Vakili, T. Gokmen, E. P. De Poortere, and M. Shayegan, Phys. Rev. Lett. **97**, 186404 (2006).

[5] I. Zutić, J. Fabian, and S. Das Sarma, Rev. Mod. Phys. **76**, 323 (2004); J. Sinova, S. O. Valenzuela, J. Wunderlich, C. H. Back, and T. Jungwirth, *ibid.* **87**, 1213 (2015).

[6] R. A. Moffatt, B. Cabrera, B. M. Corcoran, J. M. Kreikebanm, P. Redl, B. Shank, J. J. Yen, B. A. Young, P. L. Brink, M. Cherry, A. Tomada, A. Phipps, B. Sadoulet, and V. M. Sundqvist, Appl. Phys. Lett. **108**, 022104 (2016).

[7] C. E. Nebel, Nat. Mater. **12**, 690 (2013); J. Isberg, M. Gabrysch, J. Hammersberg, S. Majdi, K. K. Kovi, and D. J. Twitchen, *ibid.* **12**, 760 (2013).

[8] S. A. Parameswaran and V. Oganesyan, Nat. Phys. **8**, 7 (2012); Z. Zhu, A. Collaudin, B. Fanqué, W. Kang, and K. Behnia, *ibid.* **8**, 89 (2012).

[9] M. Padmanabhan, T. Gokmen, and M. Shayegan, Phys. Rev. Lett. **104**, 016805 (2010).

[10] K. Eng, R. N. McFarland, and B. E. Kane, Phys. Rev. Lett. **99**, 016801 (2007); R. N. McFarland, T. M. Kott, L. Sun, K. Eng, and B. E. Kane, Phys. Rev. B **80**, 161310(R) (2009); T. M. Kott, B. Hu, S. H. Brown, and B. E. Kane, *ibid.* **89**, 041107(R) (2014).

[11] E. H. Hwang and S. Das Sarma, Phys. Rev. B **87**, 075306 (2013).

[12] F. Amet and G. Finkelstein, Nat. Phys. **11**, 989 (2015); Y. Shimazaki, M. Yamamoto, I. V. Borzenets, K. Watanabe, T. Taniguchi, and S. Tarucha, *ibid.* **11**, 1032 (2015) M. Sui, G. Chen, L. Ma, W.-Y. Shan, D. Tian, K. Watanabe, T. Taniguchi, X. Jiu, W. Yao, and Y. Zhang, *ibid.* **11**, 1027 (2015).

[13] R. V. Gorbachev, J. C. W. Song, G. L. Yu, A. V. Kretinin, F. Withers, Y. Cao, A. Mishchenko, L. V. Grigorieva, K. S. Novoselov, L. S. Levitov, and A. K. Geim, Science **346**, 448 (2014); R. V. Gorbachev, F. V. Tikhonenko, A. S. Mayorov, D. W. Horsell, and A. K. Savchenko, Phys. Rev. Lett. **98**, 176805 (2007).

[14] J. Lee, K. F. Mak, and J. Shan, Nat. Nanotechnol. **11**, 421 (2016).

[15] K. F. Mak, K. L. McGill, J. Park, and P. L. McEuen, Science **344**, 1489 (2014).

[16] J. Lee, Z. Wang, H. Xie, K. F. Mak, and J. Shan, Nat. Mater. **16**, 887 (2017).

[17] S. Wu, J. S. Ross, G.-B. Liu, G. Aivazian, A. Jones, Z. Fei, W. Zhu, D. Xiao, W. Yao, D. Cobden, and X. Xu, Nat. Phys. **9**, 149 (2013).

[18] H. Schmidt, F. Giustiniano, and G. Eda, Chem. Soc. Rev. **44**, 7715 (2015).

[19] T. Y. T. Hung, K. Y. Camasari, S. Zhang, P. Upadhyaya, and Z. Chen, Sci. Adv. **5**, eaau6478 (2019).

[20] J. C. W. Song and M. A. Kats, Nano Lett. **16**, 7346 (2016).

[21] J. Xin, Y. Tang, Y. Liu, X. Zhao, H. Pan, and T. Zhu, npj Quantum Mater. **3**, 9 (2018).

[22] Z. M. Yu, S. Guan, X.-L. Sheng, W. Gao, and S. A. Yang, Phys. Rev. Lett. **124**, 037701 (2020).

[23] Y. S. Ang, S. A. Yang, C. Zhang, Z. Ma, and L. K. Ang, Phys. Rev. B **96**, 245410 (2017).

[24] J. Qu, X. Peng, C. Luo, and J. Zhong, Mater. Res. Express **4**, 105032 (2017).

[25] D. Xiao, G.-B. Liu, W. Feng, X. Xu, and W. Yao, Phys. Rev. Lett. **108**, 196802 (2012).

[26] S. Wang, F. R. Pratama, M. S. Ukhtary, and R. Saito, Phys. Rev. B **101**, 081414(R) (2020).

[27] X. Xu, W. Yao, D. Xiao, and T. F. Heinz, Nat. Phys. **10**, 343 (2014).

[28] V. N. Smelyanskiy, A. G. Petukhov, and V. V. Osipov, Phys. Rev. B **72**, 081304(R) (2005).

[29] J. Salfi, J. A. Mol, R. Rahman, G. Klimeck, M. Y. Simmons, L. C. L. Hollenberg, and S. Rogge, Nat. Mater. **13**, 605 (2014).

[30] G. Y. Wu, N.-Y. Lue, and L. Chang, Phys. Rev. B **84**, 195463 (2011).

[31] Y. G. Semenov and K. W. Kim, Phys. Rev. B **93**, 041414(R) (2016).

[32] R. Carrillo-Bastos, C. León, D. Faria, A. Latgé, E. Y. Andrei, and N. Sandler, Phys. Rev. B **94**, 125422 (2016); Y. Jiang, T. Low, K. Chang, M. I. Katsnelson, and F. Guinea, Phys. Rev. Lett. **110**, 046601 (2013); M. Shayegan, E. P. De Poortere, O. Gunawan, Y. P. Shkolnikov, E. Tutuc, and K. Vakili, Phys. Status Solidi B **243**, 3629 (2006).

[33] H. Y. Tian and J. Wang, J. Phys.: Condens. Matter **29**, 385401 (2017).

[34] M. Settnes, S. R. Power, M. Brandbyge, and A.-P. Jauho, Phys. Rev. Lett. **117**, 276801 (2016).

[35] Y. Kim and J. D. Lee, Nano Lett. **19**, 4166 (2019).

[36] J. Jeon, Y. Kim, and J. D. Lee, Phys. Rev. Appl. **15**, 024020 (2021).

[37] E. I. Rashba, Z. S. Gribnikov, and V. Ya. Kravchenko, Sov. Phys. Usp. **19**, 361 (1976) [Usp. Fiz. Nauk **119**, 3 (1976)].

[38] D. Xiao, M.-C. Chang, and Q. Niu, Rev. Mod. Phys. **82**, 1959 (2010).

[39] D. Xiao, W. Yao, and Q. Niu, Phys. Rev. Lett. **99**, 236809 (2007).

[40] V. Yamomoto, Y. Shimazaki, I. V. Borzenets, and S. Tarucha, J. Phys. Soc. Jpn. **84**, 121006 (2015).
[41] K.-L. Chiu and Y. Xu, Phys. Rep. **669**, 1 (2017).
[42] I. D'Amico and G. Vignale, Phys. Rev. B **65**, 085109 (2002).
[43] M. Beconcini, F. Taddei, and M. Polini, Phys. Rev. B **94**, 121408(R) (2016).
[44] A. A. Andronov, A. A. Vitt, and S. E. Khaikin, *Theory of Oscillators* (Pergamon, Oxford, 1966), Chap. 2, p. 74.
[45] See Supplemental Material at http://link.aps.org/supplemental/10.1103/PhysRevB.104.075403 for the linear approximation, influence of a transverse current, and excess space-charge regions.
[46] C. M. Bender and S. A. Orszag, *Advanced Mathematical Methods for Scientists and Engineers I: Asymptotic Methods and Perturbation Theory* (Springer, Berlin, 1999), Chap. 9, p. 419.
[47] O. D. Kellogg, *Foundations of Potential Theory* (Springer, Berlin, 1967), Chap. 6, p. 172.
[48] G. A. Korn and T. M. Korn, *Mathematical Handbook for Scientists and Engineers: Definitions, Theorems, and Formulas for Reference and Review* (McGraw-Hill, New York, 1968), Chap. 15, p. 515.
[49] A. A. Grinberg, S. Luryi, M. R. Pinto, and N. L. Schryer, IEEE Trans. Electron. Devices **36**, 1162 (1989).
[50] V. A. Sydoruk, I. Zadorozhnyi, H. Hardtdegen, H. Luth, M. V. Petrychuk, A. V. Naumov, V. V. Korotyeyev, V. A. Kochelap, A. E. Belyaev, and S. A. Vitusevich, Nanotechnology **28**, 135204 (2017).
[51] A. D. Polyanin and A. V. Monzhirov, *Handbook of Integral Equations*, 2nd ed. (CRC Press, Boca Raton, FL, 2008), Chap. 14, p. 707.
[52] M. Ersfeld, F. Volmer, L. Rathmann, L. Kotevitz, M. Heithoff, M. Lohmann, B. Yang, K. Watanabe, T. Taniguchi, L. Bartels, J. Shi, C. Stampfer, and B. Beschoten, Nano Lett. **20**, 3147 (2020).
[53] J. Kim, C. Jin, B. Chen, H. Cai, T. Zhao, P. Lee, S. Kahn, K. Watanabe, T. Taniguchi, S. Tongay, M. F. Crommie, and F. Wang, Sci. Adv. **3**, e1700518 (2017).
[54] A. Rycerz, J. Tworzidlo, and C. W. J. Beenakker, Nat. Phys. **3**, 172 (2007).
[55] K. I. Sasaki and K. Wakabayashi, Phys. Rev. B **82**, 035421 (2010).
[56] Z. S. Gribnikov, V. A. Kochelap, and E. I. Rashba, Sov. Phys.–JETP **24**, 178 (1967) [Zh. Eksp. Teor. Phys. **51**, 266 (1966)].
[57] V. A. Kochelap and V. N. Sokolov, J. Appl. Phys. **127**, 224302 (2020).
[58] O. E. Raichev, G. M. Gusev, A. D. Levin, and A. K. Bakarov, Phys. Rev. B **101**, 235314 (2020).
[59] K. Moors, A. Contino, M. L. Van de Put, W. G. Vandenberghe, M. V. Fischetti, W. Magnus, and B. Sorée, Phys. Rev. Mater. **3**, 024001 (2019).
[60] E. J. McCormic, M. J. Newburger, Y. K. Luo, K. M. McCreary, S. Singh, I. B. Martin, E. J. Cichewicz, Jr., B. T. Jonker, and R. K. Kawakami, 2D Mater. **5**, 011010 (2018).
[61] W. Melitz, J. Shen, A. C. Kummel, and S. Lee, Surf. Sci. Rep. **66**, 1 (2011).
[62] X.-P. Zhang, C. Huang, and M. A. Cazalilla, 2D Mater. **4**, 024007 (2017).
[63] N. A. Sinitsyn, J. Phys.: Condens. Matter **20**, 023201 (2008).
[64] A. Kormányos, G. Burkard, M. Gmitra, J. Fabian, V. Zólyomi, N. D. Drummond, and V. Fal'ko, 2D Mater. **2**, 022001 (2015).